Published in final edited form as:

Nat Methods. 2011 January ; 8(1): 91–96. doi:10.1038/nmeth.1543.

Stabilized Imaging of Immune Surveillance in the Mouse Lung

Mark R. Looney[1,2,5], **Emily E. Thornton**[3,5], **Debasish Sen**[3], **Wayne J. Lamm**[4], **Robb W. Glenny**[4], and **Matthew F. Krummel**[3]

[1]Department of Medicine, University of California, San Francisco

[2]Department of Laboratory Medicine, University of California, San Francisco

[3]Department of Pathology, University of California, San Francisco

[4]Department of Medicine, University of Washington

Abstract

Real-time imaging of cellular and sub-cellular dynamics in vascularized organs requires image-resolution, image-registration, and demonstrably intact physiology to be simultaneously optimized. This problem is particularly pronounced in the lung in which cells may transit at speeds > 1 mm/sec, and in which normal respiration results in large-scale tissue movements that prevent image registration. Here, we report video-rate, two-photon imaging of a physiologically intact preparation of the mouse lung that is at once stabilizing and non-disruptive. The application of our method provides evidence for differential trapping of T cells and neutrophils in mouse pulmonary capillaries and enables observation of neutrophil mobilization and dynamic vascular leak in response to stretch and inflammatory models of lung injury in mice. The system permits physiological measurement of motility rates of > 1 mm/sec, observation of detailed cellular morphology, and could be applied to other organs and tissues while maintaining intact physiology.

INTRODUCTION

The lung is a unique organ with an air-liquid interface exposing it to the environment and to a large volume of blood that transits the organ each minute. The lung microcirculation is also distinctive with a rich network of capillary segments with diameters as small as a few microns, which requires many leukocytes to deform their shape to pass through1. In fact, as compared to systemic vascular beds, the initial sequestration of neutrophils in the lung microcirculation is more dependent on mechanical forces than adhesion-mediated rolling along the endothelial surfaces2. Any perturbation to the integrity of the lung's air-liquid

Corresponding Author: Matthew F. Krummel, Ph.D. 513 Parnassus Avenue, HSW 512 San Francisco, CA 94143-0511 matthew.krummel@ucsf.edu Tel: (415) 514-3130 Fax: (415) 514-3165.

[5]Co-first authors

AUTHOR CONTRIBUTIONS M.R.L. conceived and designed the experiment, validated and implemented the technique, collected and analyzed data and wrote the manuscript. E.E.T. conceived and designed the experiment, validated and implemented the technique, collected and analyzed data and wrote the manuscript. D.S. implemented the technique, collected and analyzed data. W.J.L. conceived and designed the experiment and validated the technique. R.W.G. conceived and designed the experiment and edited the manuscript. M.F.K. conceived and designed the experiment, provided administrative and financial support and wrote the manuscript.

COMPETING FINANCIAL INTERESTS The authors have no competing financial interests.

interface can have devastating consequences resulting in lung vascular leak and compromised gas exchange. Furthermore, the nature of the collaboration between immune cells and structural elements of the lung has been inaccessible for real-time analysis.

The uniqueness of the lung requires direct imaging, however this demands both fast, high-resolution, and penetrant imaging methodologies as well as demonstrable maintenance of intact physiology. The lung provides a particular challenge as it propagates motion due to cardiac contractions, pulsatile blood flow, and significant overall movements during the inhalation/exhalation cycle3. Compared to the submicron resolution demanded by analysis of deformability, these movements are on the scale of millimeters when measured at the pleural face of the lung. Previous protocols for imaging in the lung have relied upon methods such as isolation and re-perfusion of the lung *ex vivo*4, clamping of ventilation5, or capturing images at end-expiration or after cessation of mechanical ventilation6. While each of these approaches has been useful for lung imaging, an improvement was needed to address high-speed 3D cellular dynamics under physiological gas exchange and blood flow.

We addressed these issues via an optimized, resonant-scanning two-photon platform7. Our method adopted point-scanning multi-photon imaging which provides excellent depth penetration. The depth (z)-resolution across numerous air-liquid alveolar interfaces severely influences the coherence of light at the focus. Multi-photon excitation, with its inherent requirement for high-photon densities, is resistant to image degradation, compared to single photon approaches. Resonant scanning permits acquisition at or exceeding video-rate8 thus providing high temporal resolution of large cross-sectional areas. Finally, and most importantly, we have optimized a gentle stabilization system which limits tissue motion, even while permitting intact blood flow at predicted rates and providing continuous access to inhaled gases. We apply this system to describe immune cell circulation and cellular movement under steady state physiology and in lung inflammation and injury models. Our results suggest surveillance of the alveolar-capillary interface from the bloodstream.

RESULTS

Experimental setup and stabilization

To stabilize the lung for imaging in a live animal with minimal disruption of ventilation or circulation, we constructed a thoracic window3,9, modified for the mouse with a 4 mm internal diameter (Fig. 1a–b). An important feature of this device is its loose adherence to the lung surface via 20–25 mmHg of reversible vacuum spread over a large local area allowing for gas to enter and expand the lung but limiting the associated movement in the x, y and z dimensions. The vacuum in this device (red arrows, Fig. 1b) circulates through grooves adjacent to the imaging area and gently pulls the tissue into a shallow conical region (blue arrows) facing an imaging-grade coverslip. The vacuum further effectively sets the coverslip in a small groove along the outside dimension of the device.

For the surgical preparation, mice were anesthetized and a tracheotomy was done to facilitate mechanical ventilation. Mice were then placed in the right, lateral decubitus position and three left anterior ribs were resected revealing the left, anterior lung surface (Fig. 1c). The thoracic suction window, attached to a rigid strut and a micromanipulator, was

then positioned immediately above the left lung and 20–25 mmHg of suction was applied to gently immobilize the lung throughout the respiratory cycle (Fig. 1d). We chose the least amount of suction that allowed the lung to enter the thoracic window and remain throughout the respiratory cycle. While the applied suction is an increase above the negative pleural pressures in the intact thorax of spontaneously breathing mice10, it would be expected to dissipate in areas further away from the window itself, thus providing limited effects well within the range of two-photon excitation. The objective was then lowered onto the 12 mm glass coverslip for imaging with our two-photon microscope (Supplementary Fig. 1a online) in the central region of this preparation to minimize any effects of suction transmitted to the edges. We tested for any damage to the lungs from mechanical ventilation or thoracic suction using the gravimetric method to measure lung edema formation. We found no increase in lung edema after 2 hours of continuous ventilation and thoracic suction (Supplementary Fig. 1b online).

To demonstrate that there is still motion associated with inhalation/exhalation, Supplementary Movie 1 shows a time-lapsed movie of alveolar inflation and deflation under suction window conditions confirming that ventilation was maintained in the portion of lung contained within the thoracic window. One of the important advantages of two-photon microscopy is tissue penetration beyond that achievable with single-photon confocal approaches. We tested the z-depth capabilities of our method by injecting Texas Red dextran intravenously and scanning down in the z-axis. We captured images at different z-depths down to 125 microns (Supplementary Fig. 1c online), which allowed for the complete visualization of the capillary bed on top of and beneath the subpleural alveoli (Fig. 1e).

We next tested the stability of images that are captured from our imaging system. Using mice that ubiquitously express CFP (actin-CFP), ventilated at 120 breaths per minute (bpm), Fig. 1f shows un-averaged still images captured at 30 frames per sec (fps) of inspiration, expiration, and inspiration again with overlay images from three subsequent timepoints, revealing that the alveolar and microvascular structures are stable with our imaging technique (see also Supplementary Movie 2). Based on the limited movement of vessels even during respiration, we estimate we have reduced overall motion to approximately 5–10 μm in all dimensions.

To quantify the stability and the deflections induced by mechanical ventilation captured at 30 fps, we used the Pearson's coefficient between frames as shown in Fig. 1f, revealing that exactly four frames per breath are disrupted due to ventilation (120 bpm), but that the image reliably returns to a stable baseline after each respiratory cycle thus giving 20 fps with exceptional `co-localization' of tissue. Time-averaging (15 integrated video-rate frames) of our image acquisition also effectively averages out the four out of sync frames due to breathing (Fig. 1g **and** Supplementary Movie 3), producing low-noise images. An alternative approach to improve image stability is to remove the four frames where breathing was occurring in post-processing (Supplementary Fig. 1d, online). We also injected intravenous Texas Red dextran (70,000 MW) into wild-type mice to visualize the lung microcirculation. These blood vessels and rather slow-moving cellular shadows within are also stably captured with our system (Supplementary Movie 4).

Perfusion and cellular behavior with thoracic suction

We next examined blood flow velocities in the lung contained within the thoracic window by intravenously injecting fluorescent microspheres (1 μm) into actin-CFP mice and tracking their movement inside microvasculature using fast acquisition rates (30 fps). In Fig 2a, an individual red fluorescent microsphere is tracked (dragon tails) during its transit through the imaging field of an 8–15 μm blood vessel. We observed a majority of beads to transit lung microvasculature at fast flow rates (109 ± 12 μm/s, mean ± s.e.m., Fig. 2b) through this small-sized blood vessel (Fig. 2a **and** Supplementary Movie 5). We also calculated bead speeds through a larger vessel (30 μm in diameter), which yielded faster flow rates of 280 ± 53 μm/s (Fig. 2b **and** Supplementary Movie 6). Our calculated perfusion velocities in these blood vessels are similar to previous reports in the lung and in systemic microvasculature not using stabilized window methods11,12.

An important advantage of intravital imaging in the mouse is the availability of fluorescent reporter strains to facilitate cellular imaging and we sought to couple our method with these in order to understand how specific cell types behave as they transit the lung. Most notably, it has not been possible to assess the degree to which neutrophils or T cells may `patrol' the vasculature, given the extremely tight constrictions during their transit. We tracked the movement of endogenous LysM-GFP^{+} neutrophils in both small capillary segments (average 10–15 μm in diameter) and in larger vessels (average 30 μm in diameter, Fig. 2c) and we report the individual transit velocities of these cells (Fig. 2d). Sequential images of neutrophils (green) transiting a medium-sized blood vessel that has also been injected with red, fluorescent microspheres (1 μm) are shown (Fig. 2c, Supplementary Movie 6). GFP^{+} neutrophils transit at 1.42 ± 0.16 μm/s in capillary segments and at 97 ± 38 μm/s in vessels roughly twice as large (Fig. 2d). However, we observed a bimodal distribution of neutrophil perfusion velocities in medium-sized vessels, with one population of neutrophils transiting at speeds just below the rate of 1 μm beads and another population transiting much slower and rolling and even arresting along the endothelial surface (Supplementary Movie 6, Fig. 2e). Some individual neutrophils remain trapped for long periods and move much more slowly even in larger-sized blood vessels, compared to the flow as calculated by the movement of much smaller beads. The heterogeneity of neutrophil transit velocities has been previously documented in the canine circulation13. In sum, this suggests both trapping in narrow capillaries but also continuous scanning of the lung vasculature under rapid flow.

We next tested the contribution of cell size or activation state to intravascular cell velocities in the lung and we observed a general trend in which larger and more activated cells move more slowly than naïve ones: naïve T cells (CD2-RFP) injected into the jugular vein move with a velocity of 2.48 ± 0.49 μm/s compared with T cells that have been activated for four days with their cognate antigen and with interleukin-2 (blasts), which transit at less than 0.5 μm/s (Fig. 3a). With the 0.6 μm resolution capacity of our two-photon microscope, we were also able to detect that small (naïve) T cells did not evidently adopt elongated `amoeboid' characteristic morphology (Fig. 3b), even while undergoing evident surveillance of the capillary (Supplementary Movie 7). In contrast, larger, stimulated T cells were not only characteristically amoeboid but also make multiple projections, likely down two vessels at a junction (Fig. 3b). Furthermore, when naïve T cells were injected i.v., we detected their

entry into the capillary segments of the lung whereas T cell blasts were restricted to larger blood vessels and largely did not enter the capillary segments (Fig. 3c–d **and** Supplementary Movie 7). This pattern of distribution was likely explained by the size differences between these two cell types (Fig. 3e).

Neutrophil dynamics in lung inflammation and injury

A significant value in our system is that the lung continues to receive ventilation as it normally would and is under normal physiological blood flow, allowing for the direct examination of events when inhaled or intravascular agents first enter the lung. We applied our imaging technique under different pathologic conditions (Fig. 4) in order to examine the cellular changes that occur as inhaled material enters the lung. We imaged LysM-GFP mice injected with Texas Red dextran before and after intratracheal challenge with the neutrophil chemokine, MIP-2 (macrophage inflammatory protein-2; 5 μg) (Fig. 4a). As predicted by end-point studies, a large influx of GFP^+ neutrophils after chemokine challenge occurred (Fig. 4b Supplementary Movie 8). Importantly, in control experiments when LysM-GFP mice were continuously ventilated under suction window conditions for 75 minutes, there was no artificial recruitment of neutrophils over time (Fig. 4c). Intratracheal challenge with MIP-2 produces a dynamic scrum of cells; we observed neutrophil crawling in the intravascular compartment, with individual cells rapidly changing their leading and trailing edges (Fig. 4d **and** Supplementary Movie 9). Additionally, we could identify mobile, extravascular neutrophils with rounded morphologies after chemokine challenge (Fig. 4e **and** Supplementary Movie 10). As this model provides global chemokine, it is perhaps not unexpected to see such active behaviors or intra-alveolar entry of cells. To examine a more physiological insult, we used a model of acute LPS inflammation and injury and identified similar neutrophil swarming after intratracheal LPS challenge (5 mg/kg, Fig. 4f–g **and** Supplementary Movie 11).

We also examined the dynamic leakage of dextran (70K MW) into the extravascular compartment, which is indicative of the increased lung vascular permeability characteristic of acute lung injury (Fig. 4h **and** Supplementary Movie 12). The averaged progressive increase in dextran leakage after intratracheal LPS was quantified, showing a differential rate of vascular leakage across the imaged alveoli (Fig. 4i, Supplementary Movie 12). In other words, some alveoli leaked faster than others, an observation that could not be made with common endpoint measurements of global lung vascular permeability.

Finally, we examined a model of ventilator-induced lung injury, an important contributor to excess mortality in critically ill patients14. We visualized and quantified dextran leakage into the interstitial and alveolar spaces in mice challenged with lung stretch compared with normal tidal volumes (Fig. 4j–k **and** Supplementary Movie 13). Again, we observed heterogeneity in the rates of vascular leak among the imaged alveoli.

DISCUSSION

The method we describe here provides demonstrably intact access to the circulation and lung microanatomy in the mouse and, with the combination of speed, sensitivity, resolution and stability, solves a number of problems that have prevented examination of important

processes in the lung. Importantly, the method does not involve interruption of ventilation with the attendant pulmonary vasoconstrictor response5 or artificial perfusion or removal of the organ from the host. Isolated, perfused lung preparations have been widely used in pulmonary research with great success and with the advantage of manipulating flow velocities and shear stresses15–17. However, this technique does not retain lymphatic flow, circulation is interrupted so that recruitment of cells from the bone marrow or lymphatic system is not possible, and perfusion through an artificial circulation may have unintended consequences on cellular behavior.

Our technique preserves both ventilation and perfusion. The rates of blood flow are similar to values presumed from other organs and there is visible evidence of ventilation, but this does not prevent imaging from taking place since the system reliably returns to its pre-inspiration/expiration resting state. Imaging throughout the respiratory cycle is a significant technical advance over prior intravital lung preparations in which imaging either occurred with the interruption of ventilation or was timed for capture at only end-expiration6. Finally, our approach is durable with no detectable injury to the stabilized lung and we were able to routinely image for up to 3 hours, which is the longest period of imaging that we have attempted thus far.

Neutrophils uniquely traverse the lung compared to other tissues13, yet much of the studies of neutrophil rheology using intravital techniques have come from non-pulmonary organs, which may not accurately reflect the dynamics of the pulmonary microcirculation18. Neutrophil-mediated lung diseases, such as acute lung injury19, can now be studied directly. Our approach also permitted us to observe capture of multiple cell-types and to measure significant dwell times for lymphocytes that reach the small capillary segments. This stalling effect may provide ample opportunity for both surveillance and also for lung-remodeling factors to be deposited; these details are now open to investigation using this approach. Indeed, the method should enable the study of both the onset of adaptive immune responses and the homing of metastatic tumors to the lung. Breast tumor metastases and indeed normal breast ductal cells may establish residency in the lung20 and it will, for the first time, be possible to study this process as it unravels and possibly identify the supporting cells of the metastatic niche.

The limitations of our system include (1) imaging under positive pressure ventilation and not during spontaneous breathing and (2) imaging of only subpleural blood vessels and alveolar units, although we are able to image up to 125 microns below the pleural surface and it is worth noting that the subpleural and deeper parenchymal microvascular networks are generally thought to be similar in terms of vascular regulation21. A recent paper using glue to fix the lung surface to a coverslip provides a possible alternative method that may have similar benefits to those presented here but the physiologic integrity of that preparation has yet to be established22. While our system substantially improves upon existing approaches, there remains room for further improvements. For example, adaptive optics has recently been used to overcome the distortions associated with changes in refractive index as two-photon light enters the target tissue23. Such an approach would undoubtedly be beneficial in the lung where light transverses many such interfaces at the surface of each subsequent air-filled alveolus. Further advances in miniaturization, such as the use of gradient index

lenses24 or miniaturized lens elements should also be possible, which may result in even less invasive approaches that are possibly suitable for diagnostic thoracic imaging in human patients.

METHODS

Mice

The following mice were used in our experiments: C57BL/6 wild-type (Charles River); *c-fms*-GFP25 in which GFP is driven under the CSF-1R promoter (highlights neutrophils, monocytes, and macrophages and were provided by Zena Werb (UCSF)); actin-CFP26 have the CFP transgene ubiquitously expressed and were obtained from I. Weissman (Stanford University); CD2-RFP (expressing RFP+ in all T cells and a small subset of NK cells), OT-II TCR transgenic (OVA-specific Class II restricted), ubiquitin-GFP (GFP expression in all cells), and LysM-GFP (GFP^+ neutrophils, monocytes, and macrophages) were obtained from The Jackson Laboratories. All experiments involving mice were approved by the Institutional Animal Care and Use Committee at the University of California, San Francisco.

Reagents

Texas Red dextran (70,000 molecular weight; Invitrogen); 1 μm, red fluorescent microspheres (Invitrogen); lipopolysaccharide (LPS) (from *Escherichia coli* O55:B5; Sigma-Aldrich); macrophage inflammatory protein-2 (MIP-2) (R&D Systems).

Thoracic suction window

We used a custom, thoracic suction window with a 4 mm internal diameter, fitted with a vacuum chamber, and accommodating a 12 mm glass coverslip.

Surgical preparation

Mice were anesthetized with Ketamine (80 mg/kg) and Xylaxine (12 mg/kg) i.p. and placed on a custom, heated microscope stage. PE-90 tubing was inserted into the trachea and sutured into place to facilitate mechanical ventilation with a rodent ventilator (Kent Scientific). Mice were ventilated with pressure control ventilation (12–15 cmH_2O), a respiratory rate of 115 breaths per minute, FiO2 of 0.5–1.0, and PEEP of 3 cmH_2O. Isoflurane was continuously delivered at 1% to maintain anesthesia and mice were given an i.p. bolus of PBS (1 ml) prior to the thoracic surgical procedure. The mice were then placed in the right lateral decubitus position and three left anterior ribs were resected and the left lung was carefully exposed. The thoracic suction window attached to a micromanipulator on the microscope stage was then placed into position and 20–25 mmHg of suction was applied (Amvex Corporation) to gently immobilize the lung. The two-photon microscope objective was then lowered into place over the thoracic suction window and a 12 mm coverslip. For intravenous injections, the right jugular vein was cannulated with a 30 gauge needle attached to PE-10 tubing for injections of cells or intravascular dyes.

Two-photon microscopy

A custom resonant-scanning 2-photon instrument7 contains a four-photomultiplier tube detector (Hamamatus R5929), collects data at video rate, and utilizes an Olympus XLUMP FL20XW (NA 0.95) objective with an overfilled back aperture with a fill-factor of approximately 1. Samples were excited with a 5-W MaiTai TiSaphire laser (Spectra-Physics) tuned to a wavelength of 910 nm, attenuated via a variable neutral density wheel to approximately 25–40% of power (0.175 – 0.28 W) and using emission wavelengths of 440/40 nm (for CFP), 505/20 nm (for GFP), and 605/70 nm (for beads or dextran) were collected. A custom, four-dimensional acquisition module in VideoSavant digital video recording software (IO Industries) or in Micromanager was utilized for image acquisition. For time-lapse acquisition, each x–y stack spans 240 μm × 288 μm at an x–y resolution of 0.6 μm per pixel. For z-stacks, we collected data at a z resolution of 2 μm. Z distances and averaged frames are indicated for each individual experiment.

Blood flow velocity experiments

Red, fluorescent microspheres (1 μm; Invitrogen) were injected into the right, jugular vein and imaged using a fast acquisition mode at 30 fps. Blood flow velocities were calculated by determining the speeds of the fastest perfusing beads through alveolar capillaries. All analyses were performed using Metamorph™ (Universal Imaging), Imaris™ (Bitplane Inc.) and Photoshop™ (Adobe Inc.) software.

Lung stretch injury

Lung stretch injury (ventilator-induced lung injury) was initiated by increasing the pressure controlled ventilation to 30 cmH_2O and decreasing the PEEP to 0 cmH_2O. Mice were also injected with Texas Red dextran (70,000 MW) via the jugular vein for the imaging of lung vascular leak.

MIP-2 and LPS-induced lung injury

Mice were intratracheally challenged with MIP-2 (5 μg; R&D Systems) or LPS from *Escherichia coli* O55:B5 (Sigma-Aldrich) at 5 mg/kg.

Quantifying lung vascular permeability

Alveolar spaces were defined by the absence of Actin CFP. Isosurfaces were drawn in the alveolar space using Imaris (Bitplane, Inc) manual surface creation tool. The relative amount of dextran within the space was determined by calculating the average red (TR dextran) intensity within the airspace.

Quantifying lung edema

The gravimetric method was used to measure the lung wet-to-dry weight ratio (grams/grams) as previously described19,27. The right and left lungs were separately removed, weighed, placed in a drying oven at 55° C for 48 hours, and then weighed again to calculate the wet-to-dry weight ratio.

T cell experiments

Activated ubiquitin-GFP OTII T cells were generated by incubating splenocytes and lymph node cells from an Ub-GFP OTII TCR transgenic mouse with ova peptide SIINFEKL (Sigma-Aldrich) and supplemented with recombinant mouse IL-2 (BD-Biosicences). They were transferred after 4 or 5 days of culture. Naïve CD2-RFP OTII cells were isolated and used immediately. A single cell suspension was isolated from lymph nodes and spleens of CD2 RFP/OTII TCR transgenic mice. Naïve CD4 T cells were purified using the Stemsep CD4 negative selection kit. T cells were transferred into actin-CFP mice via the jugular vein.

Statistics

Data is presented as mean ± standard error of the mean (s.e.m.). P values were determined by performing a two-tailed T test. To determe the stability of the imaging setup, Pearson's correlation coefficient of actin-CFP fluorescence intensity was measured for every frame with respect to the first frame, using the `co-localization' function in Imaris™.

Supplementary Material

Refer to Web version on PubMed Central for supplementary material.

ACKNOWLEDGMENTS

We thank O. Khan for his side-view rendering of the thoracic suction window and Nenad Amodaj for software support. This work was supported in part by US National Institutes of Health grants K08 HL082742 (M.R.L.) and PO1 HL024136 (M.F.K.), by the American Asthma Foundation and Sandler Basic Asthma Research Center (M.F.K.), by the National Blood Foundation (M.R.L.), and by the National Science Foundation Graduate Research Fellowships Program (E.E.T.).

REFERENCES

1. Wiggs BR, et al. Contributions of capillary pathway size and neutrophil deformability to neutrophil transit through rabbit lungs. J. Appl. Physiol. 1994; 77:463–470. [PubMed: 7961270]
2. Burns AR, Smith CW, Walker DC. Unique structural features that influence neutrophil emigration into the lung. Physiol. Rev. 2003; 83:309–336. [PubMed: 12663861]
3. Wagner WW Jr. Pulmonary microcirculatory observations in vivo under physiological conditions. J. Appl. Physiol. 1969; 26:375–377. [PubMed: 5773180]
4. Kiefmann R, Rifkind JM, Nagababu E, Bhattacharya J. Red blood cells induce hypoxic lung inflammation. Blood. 2008; 111:5205–5214. [PubMed: 18270324]
5. Hasegawa A, et al. Color-coded real-time cellular imaging of lung T-lymphocyte accumulation and focus formation in a mouse asthma model. J. Allergy Clin. Immunol. 125:461–468. e466. [PubMed: 20031194]
6. Tabuchi A, Mertens M, Kuppe H, Pries AR, Kuebler WM. Intravital microscopy of the murine pulmonary microcirculation. J. Appl. Physiol. 2008; 104:338–346. [PubMed: 18006870]
7. Bullen A, Friedman RS, Krummel MF. Two-photon imaging of the immune system: a custom technology platform for high-speed, multicolor tissue imaging of immune responses. Curr. Top. Microbiol. Immunol. 2009; 334:1–29. [PubMed: 19521679]
8. Nguyen QT, Callamaras N, Hsieh C, Parker I. Construction of a two-photon microscope for video-rate Ca(2+) imaging. Cell Calcium. 2001; 30:383–393. [PubMed: 11728133]
9. Lamm WJ, Bernard SL, Wagner WW Jr. Glenny RW. Intravital microscopic observations of 15-microm microspheres lodging in the pulmonary microcirculation. J. Appl. Physiol. 2005; 98:2242–2248. [PubMed: 15705726]

10. Hoffman AM, et al. Matrix modulation of compensatory lung regrowth and progenitor cell proliferation in mice. Am. J. Physiol. Lung Cell. Mol. Physiol. 298:L158–168. [PubMed: 19915155]
11. Popel AS, P.C. J. Microcirculation and Hemorheology. Annu. Rev. Fluid Mech. 2005; 37:43–69. [PubMed: 21151769]
12. Waisman D, et al. Subpleural microvascular flow velocities and shear rates in normal and septic mechanically ventilated rats. Shock. 2006; 26:87–94. [PubMed: 16783203]
13. Gebb SA, et al. Sites of leukocyte sequestration in the pulmonary microcirculation. J. Appl. Physiol. 1995; 79:493–497. [PubMed: 7592208]
14. Ventilation with lower tidal volumes as compared with traditional tidal volumes for acute lung injury and the acute respiratory distress syndrome. The Acute Respiratory Distress Syndrome Network. N. Engl. J. Med. 2000; 342:1301–1308. [PubMed: 10793162]
15. Presson RG Jr. Baumgartner WA Jr. Peterson AJ, Glenny RW, Wagner WW Jr. Pulmonary capillaries are recruited during pulsatile flow. J. Appl. Physiol. 2002; 92:1183–1190. [PubMed: 11842057]
16. Kuebler WM, Ying X, Singh B, Issekutz AC, Bhattacharya J. Pressure is proinflammatory in lung venular capillaries. J. Clin. Invest. 1999; 104:495–502. [PubMed: 10449441]
17. Bhattacharya J, Staub NC. Direct measurement of microvascular pressures in the isolated perfused dog lung. Science. 1980; 210:327–328. [PubMed: 7423192]
18. Zarbock A, Ley K. New insights into leukocyte recruitment by intravital microscopy. Curr. Top. Microbiol. Immunol. 2009; 334:129–152. [PubMed: 19521684]
19. Looney MR, Su X, Van Ziffle JA, Lowell CA, Matthay MA. Neutrophils and their Fc gamma receptors are essential in a mouse model of transfusion-related acute lung injury. J. Clin. Invest. 2006; 116:1615–1623. [PubMed: 16710475]
20. Podsypanina K, et al. Seeding and propagation of untransformed mouse mammary cells in the lung. Science. 2008; 321:1841–1844. [PubMed: 18755941]
21. Short AC, et al. Pulmonary capillary diameters and recruitment characteristics in subpleural and interior networks. J. Appl. Physiol. 1996; 80:1568–1573. [PubMed: 8727541]
22. Kreisel D, et al. In vivo two-photon imaging reveals monocyte-dependent neutrophil extravasation during pulmonary inflammation. Proc. Natl. Acad. Sci. U S A. 2010; 107:18073–18078. [PubMed: 20923880]
23. Ji N, Milkie DE, Betzig E. Adaptive optics via pupil segmentation for high-resolution imaging in biological tissues. Nat. Methods. 2010; 7:141–147. [PubMed: 20037592]
24. Barretto RP, Messerschmidt B, Schnitzer MJ. In vivo fluorescence imaging with high-resolution microlenses. Nat. Methods. 2009; 6:511–512. [PubMed: 19525959]
25. Sasmono RT, et al. A macrophage colony-stimulating factor receptor-green fluorescent protein transgene is expressed throughout the mononuclear phagocyte system of the mouse. Blood. 2003; 101:1155–1163. [PubMed: 12393599]
26. Hadjantonakis AK, Macmaster S, Nagy A. Embryonic stem cells and mice expressing different GFP variants for multiple non-invasive reporter usage within a single animal. BMC Biotechnol. 2002; 2:11. [PubMed: 12079497]
27. Fukuda N, Folkesson HG, Matthay MA. Relationship of interstitial fluid volume to alveolar fluid clearance in mice: ventilated vs. in situ studies. J. Appl. Physiol. 2000; 89:672–679. [PubMed: 10926653]

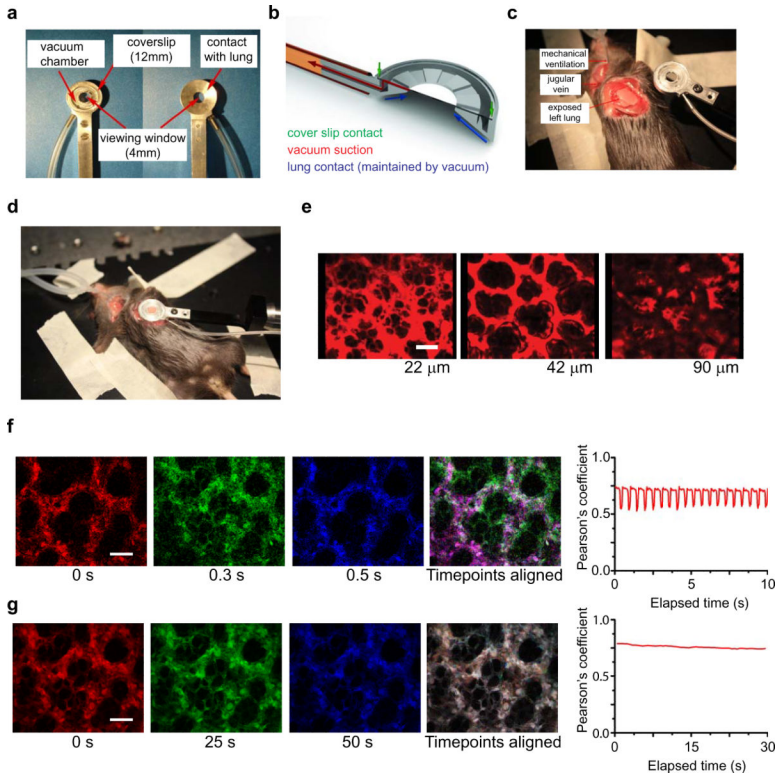

Figure 1.

Experimental setup and image stability for intravital imaging of the mouse lung. (**a**) Anterior and posterior views of the thoracic suction window fitted with a coverslip. (**b**) Side-view rendering of the suction window showing suction chamber, cover slip (green arrows) and vacuum flows (blue arrows near tissue, red arrows toward suction regulator). (**c**) Surgical preparation of left thorax with exposed left lung. (**d**) Suction window *in situ*. (**e**) Representative images at the indicated depths in a mouse injected with Texas Red dextran, showing the capillary bed above and below the subpleural alveoli (left to right). Scale bar = 50 μm (**f–g**) Still images of CFP fluorescence in an actin-CFP mouse lung at three time points, coded respectively as red, green and blue. Images were captured at 30 fps; in (**f**) each timepoint from (g) is aligned to produce a merged image. The plot shows the Pearson's coefficient from a 30 fps video over time. See also Supplementary Movie 2. (**g**), each frame represents 15 integrated images that are then merged (timepoints aligned). Scale bar = 50 μm. The plot shows the Pearson's coefficient over time from a video taken using the 15 integrated image acquisition. See also Supplementary Movie 3.

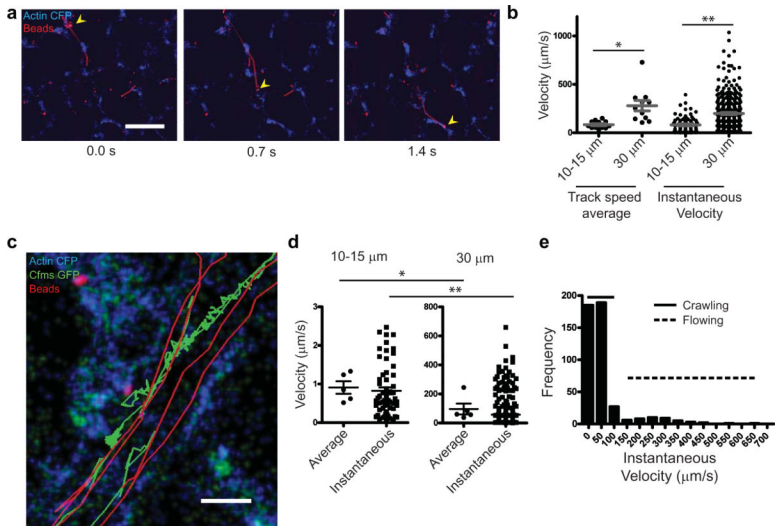

Figure 2.

Perfusion velocities of beads and neutrophils in the lung. (**a**) The micrographs show sequential images of individual beads traversing the lung microcirculation (yellow arrow heads), in actin-CFP mice injected i.v. with red fluorescent microspheres and then imaged at 30 fps. Time elapsed after the first frame is indicated. Scale bar = 50 μm. See also Supplementary Movie 5. (**b**) The plot shows perfusion velocities of individual beads in small (109 ± 12 μm/s, mean ± s.e.m., n = 14) and medium-sized blood vessels (280 ± 53 μm/s, mean ± s.e.m., n = 11, $P < 0.001$). Instantaneous = instantaneous bead speeds. Average = average speed of individual beads. (**c**) The micrograph shows four representative tracks of neutrophils (green) and beads (red) inside a vessel of an Actin-CFP/*c-fms*+ mouse injected with fluorescent microspheres and imaged at 30 fps. Scale bar = 10 μm. (**d**) The plots show the average and instantaneous speed of neutrophils in small (0.91 ± 0.16 μm/s, mean ± s.e.m., n = 5) and medium-sized (96.5 ± 37.8 μm/s, mean ± s.e.m., n = 5, $P < 0.05$) blood vessels. (**e**) Histogram of neutrophil perfusion velocities in a medium-sized blood vessel. **See also** Supplementary Movie 6.

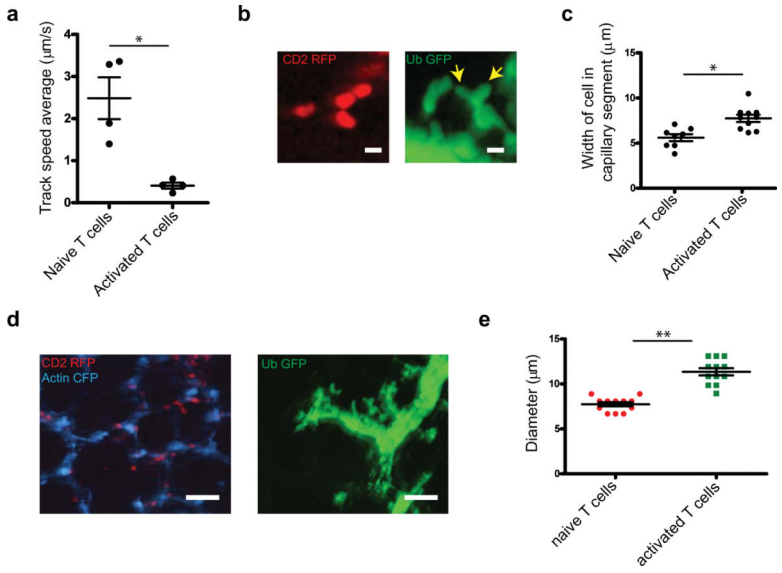

Figure 3.

Perfusion velocities of T cells in the lung. (**a**) Track speed averages of naïve (2.48 ± 0.49 μm/s, mean ± s.e.m., $n = 4$) and activated T cells (0.41 ± 0.07 μm/s, mean ± s.e.m., $n = 4$, $P < 0.01$) injected into the jugular vein of actin-CFP mice are plotted. See also Supplementary Movie 7. (**b**) Representative images showing the morphology of naïve T cells (CD2 RFP) and T cell blasts (ubiquitin-GFP). Yellow arrows indicate a T cell blast with two leading edges, likely extending into two vascular branches. Scale bar = 10 μm. (**c**) Width of the capillary segments containing naïve (5.61 ± 0.39 μm, mean ± s.e.m., $n = 8$) and activated T cells (7.75 ± 0.41 μm, mean ± s.e.m., $n = 12$, $P < 0.01$) are plotted. (**d**) Still images showing the sizes of intravascular naïve (left panel) and activated (blasts; right panel) T cells. Scale bar = 50 μm, 40 μm Z stack. (**e**) Average diameters of naïve (7.74 ± 0.23 μm, mean ± s.e.m., $n = 12$) and activated T cells (11.36 ± 0.40 μm, mean ± s.e.m., $n = 12$, $P < 0.0001$).

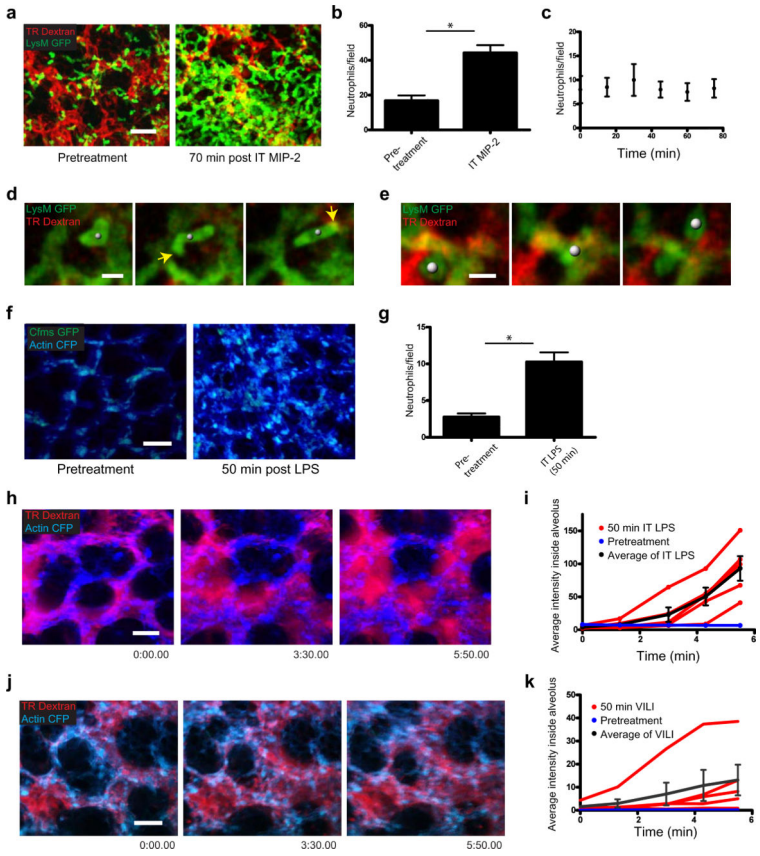

Figure 4.

Imaging inflammation and injury-induced neutrophil dynamics in physiologically intact lungs. (**a**) Images of the lung of a LysM-GFP mouse injected with Texas Red dextran and imaged before (left panel) and after (right panel) intratracheal instillation of MIP-2. Scale bar = 50 μm, 40 μm z stack. See also Supplementary Movie 8. (**b**) Number of GFP+ neutrophils in the imaging field before (16.75 ± 3.06 cells, mean ± s.e.m., $n = 4$) and after MIP-2 (44.25 ± 4.42 cells, mean ± s.e.m., $n = 4$, $P < 0.01$) instillation. (**c**) Number of GFP+ neutrophils in the lung vasculature under continuous suction ($n = 4$ for each timepoint). (**d**) Representative images of an intravascular GFP^+ neutrophil. Scale bar = 10 μm, single z plane at 5:20, 6:40 and 9:20 min:sec. (**e**) Representative images of a GFP^+ neutrophil moving within alveoli. Scale bar = 10 μm, single z plane at 0:40, 5:40 and 9:00 min:sec. See also Supplementary Movie 10. (**f**) Images of the lung of an actin-CFP/*c-fms*-GFP mouse before and after intratracheal instillation of LPS. Scale bar = 50 μm, 40 μm z stack. See also Supplementary Movie 11. (**g**) Number of neutrophils per field before (2.75 ± 0.48, mean ± s.e.m., $n = 4$) and after LPS instillation (10.25 ± 1.32, mean ± s.e.m., $n = 4$, $P < 0.01$). (**h, j**) Images of the lung of an actin-CFP mouse injected with Texas Red dextran and either challenged with intratracheal LPS for 50 minutes (**h**) or subjected to ventilator-induced lung injury for 60 minutes (**j**). Scale bar = 50 μm, 40 μm z stack. See also Supplementary Movie 12, 13. (**i, k**) The plots shows the average intensity of fluorescent dextran in the alveolar space at the indicated times after LPS treatment (**i**) or ventilator-induced lung injury (**k**).

Blue lines are the pre-treatment average (n = 3 alveoli), red lines are individual alveoli measured post-treatment, and black lines are the post-treatment average (n = 5 alveoli).